The Astrophysical Journal, 934:103 (17pp), 2022 August 1 https://doi.org/10.3847/1538-4357/ac78df

Quantitative Characterization of Magnetic Flux Rope Properties for Two Solar Eruption Events

Wen He[1], Qiang Hu[1,2], Chaowei Jiang[3], Jiong Qiu[4], and Avijeet Prasad[5,6]
[1] Department of Space Science, The University of Alabama in Huntsville, Huntsville, AL 35805, USA
[2] Center for Space Plasma and Aeronomic Research (CSPAR), The University of Alabama in Huntsville, Huntsville, AL 35805, USA; qh0001@uah.edu
[3] Institute of Space Science and Applied Technology, Harbin Institute of Technology, Shenzhen, People's Republic of China
[4] Physics Department, Montana State University, Bozeman, MT 59717, USA
[5] Institute of Theoretical Astrophysics, University of Oslo, Postboks 1029 Blindern, NO-0315 Oslo, Norway
[6] Rosseland Centre for Solar Physics, University of Oslo, Postboks 1029 Blindern, NO-0315 Oslo, Norway
Received 2022 January 7; revised 2022 May 21; accepted 2022 June 13; published 2022 July 28

Abstract

In order to bridge the gap between heliospheric and solar observations of coronal mass ejections (CMEs), one of the key steps is to improve the understanding of their corresponding magnetic structures like the magnetic flux ropes (MFRs). But it remains a challenge to confirm the existence of a coherent MFR before or upon the CME eruption on the Sun and to quantitatively characterize the CME-MFR due to the lack of direct magnetic field measurements in the corona. In this study, we investigate MFR structures originating from two active regions (ARs), AR 11719 and AR 12158, and estimate their magnetic properties quantitatively. We perform nonlinear force-free field extrapolations with preprocessed photospheric vector magnetograms. In addition, remote-sensing observations are employed to find indirect evidence of MFRs on the Sun and to analyze the time evolution of magnetic reconnection flux associated with the flare ribbons during the eruption. A coherent "preexisting" MFR structure prior to the flare eruption is identified quantitatively for one event from the combined analysis of the extrapolation and observation. Then the characteristics of MFRs for two events on the Sun before and during the eruption forming the CME-MFR, including the axial magnetic flux, field line twist, and reconnection flux, are estimated and compared with the corresponding in situ modeling results. We find that the magnetic reconnection associated with the accompanying flares for both events injects a significant amount of flux into the erupted CME-MFRs.

Unified Astronomy Thesaurus concepts: Solar coronal mass ejections (310); Solar flares (1496); Solar active region magnetic fields (1975); Solar magnetic fields (1503)

1. Introduction

Coronal mass ejections (CMEs) are spectacular eruptions of plasma often accompanied by rapid release of magnetic energy from the solar atmosphere. When CMEs propagate away from the Sun to interplanetary space, they are often called interplanetary CMEs (ICMEs), which exhibit a distinct set of observational signatures from in situ measurements. They are recognized as drivers of major space weather events that could severely impact human activity in modern society. Erupted flares have a close relationship with CMEs and strong flares are often observed along with CMEs (Chen 2011). In the past few decades, a lot of efforts have been made on the development of the flare–CME model in order to explain the underlying physical mechanism(s). Among them, the standard two-dimensional (2D) flare and CME model, the so-called CSHKP model (developed by Carmichael 1964; Sturrock 1966; Hirayama 1974; Kopp & Pneuman 1976), has successfully explained the morphological evolution of eruptive two-ribbon flares. One of the essential components in the model is the CME magnetic flux rope (MFR). Upon its ejection, field lines below the erupting rope reconnect and form an arcade of flare loops observed in X-ray and extreme ultraviolet (EUV) wavelengths, and two ribbons observed in optical and ultraviolet (UV) wavelengths demarcating the feet of the arcade. In the 2D model, the same amount of magnetic flux encompassed by the flare loops is also turned into poloidal flux of the erupting MFR, and this amount of flux can be measured from flare ribbons sweeping through the photospheric magnetic field (Forbes & Priest 1984; Qiu et al. 2004, 2007). Since MFRs are generally believed to be the core magnetic structure of CMEs and ICMEs (e.g., Gibson et al. 2006; Hu et al. 2014; Gopalswamy et al. 2017, 2018; Liu 2020), properties of MFRs related to their formation and evolution remain an important topic to explore. We note that hereafter we use "MFR" for a more generic reference to an MFR at different stages of evolution, and "CME-MFR" for specific reference to an MFR at the final stage of CME eruption (i.e., when the MFR has well formed after flare reconnection).

Today, the study of the evolution and propagation of CMEs/ICMEs between the Sun and the Earth has greatly advanced with the help of multiple measurements from multi-spacecraft missions. The large-scale magnetic clouds (MCs) in ICMEs, which are commonly detected in situ, provide direct evidence for the existence of erupted CME-MFRs that come from the Sun (Burlaga 1992; Qiu et al. 2007; Hu et al. 2014). In addition, there are remote-sensing observations available throughout interplanetary space. For example, the twin spacecraft Solar Terrestrial Relations Observatory (STEREO; Kaiser et al. 2008) can trace CMEs from the high corona to the inner heliosphere via coronagraphic observations. The STEREO mission provides two viewpoints toward the Sun, in addition to the viewpoint from Earth provided by the Solar and Heliospheric Observatory (SOHO) in past decades. There are also various signatures for

MFRs on the Sun from remote-sensing observations, including filaments, coronal cavities, sigmoids, and hot channels (Cheng et al. 2017). These solar phenomena can be unified into one framework as distinct manifestations of MFRs (Liu 2020). Most of the latest recognized observational features are attributed to observations from the Solar Dynamics Observatory (SDO; Pesnell et al. 2012). The recent development of large ground-based solar telescopes has also become an indispensable way to reveal the fine-scale structures and dynamics of MFR formation in the low corona (e.g., Wang et al. 2015).

Compared to various studies based on in situ measurements of MFR structures after eruption, the origination of CME-MFRs before and during eruptions remains elusive due to the complex environment in the solar source region and limited observations. At the present time, there are certain hypotheses on the formation process of MFRs. Some studies indicate that MFRs could exist prior to the eruption. For example, both Fan (2001) and Magara (2004) reported findings from magnetohydrodynamic (MHD) simulation that a twisted MFR initially formed below the photosphere can partially emerge into the low corona by magnetic buoyancy. Other studies suggest that the presence of preeruptive MFRs is not necessary and MFRs could be built up in the corona via magnetic reconnection processes associated with flares (Amari et al. 2003; Moore et al. 2001; Antiochos et al. 1999; Jiang et al. 2021a, 2021b). To understand the physical processes more precisely for flare–CME events, extensions of the standard 2D flare model have been proposed to account for much broader ranges of quantitative measurements with three-dimensional (3D) features intrinsic to realistic solar eruptions (Longcope et al. 2007; Aulanier et al. 2012; Priest & Longcope 2017; Aulanier & Dudík 2019). For example, quasi-3D models have been developed with a nonvanishing magnetic field component along the axis of the MFR and to illustrate the scenario that sequential reconnection along the magnetic polarity inversion line (PIL) forms the MFR in the first place (van Ballegooijen & Martens 1989; Longcope et al. 2007; Schmieder et al. 2015). This scenario has been widely applied to infer and interpret magnetic reconnection properties based on the observed flare ribbon morphology (Qiu et al. 2002, 2004, 2010; Hu et al. 2014; Kazachenko et al. 2017; Zhu et al. 2020). From such analyses, Qiu et al. (2004) illustrated that there is a temporal correlation between the magnetic reconnection rate and the acceleration of the CME (considered as the eruptive MFR) in the low corona. Such a correlation has been further established by Zhu et al. (2020) based on a statistical study of ∼60 events. In addition, Qiu et al. (2007) and Hu et al. (2014) showed a correlation between the magnetic reconnection flux and the flux contents of the corresponding ICME/MC flux ropes based on modeling results employing in situ spacecraft measurements. These results support the hypothesis that CME-MFRs can be formed by magnetic reconnection during the corresponding flare process. Recent simulation results also indicate clearly that the reconnection flux contributes to the axial (toroidal) flux of the CME-MFR in the early stage (Jiang et al. 2021a; Inoue et al. 2018).

For quantitative MFR identification in the solar source region, numerical models can be applied to find MFRs in addition to observations. For the topological analysis of a solar MFR, the 3D magnetic field configuration is commonly obtained through coronal magnetic field extrapolation based on photospheric magnetograms. A number of high-resolution extrapolation results employing different numerical schemes have been compared to observations to study the properties of MFRs in the magnetically dominant environment on the Sun (Schrijver et al. 2008; Thalmann et al. 2008; Wheatland & Régnier 2009; De Rosa et al. 2009; Wiegelmann et al. 2012; Sun et al. 2012; Jiang et al. 2014; Guo et al. 2016). Among many extrapolation studies, the force-free approximation is commonly adopted for the case of low plasma β (the ratio between the plasma pressure and magnetic pressure) over certain heights in the solar atmosphere above the photosphere (Gary 2001). Under this assumption, nonmagnetic forces including the inertial force can be ignored for a static and time-stationary equilibrium. Therefore, the Lorentz force should be self-balanced, and it should satisfy the equation $\boldsymbol{J} \times \boldsymbol{B} = 0$, which means that the electric current density $\boldsymbol{J}$ is parallel to the magnetic field $\boldsymbol{B}$, with $\boldsymbol{J} = \alpha \boldsymbol{B}$ (α is the so-called force-free parameter). The simplest case is the potential field when $\alpha \equiv 0$. If α is not zero, there are two situations depending on whether α is constant or varying in space. One is the linear force-free field for $\alpha \equiv$ const and the other is the nonlinear force-free field (NLFFF). Since our interest lies in the magnetic structure in active regions (ARs) on a local scale with high spatial resolution, the most common and practical way to reconstruct the coronal magnetic field is the NLFFF extrapolation method.

There are a variety of numerical methods proposed to reconstruct the NLFFF for an AR from boundary conditions and sometimes pseudoinitial conditions, including upward integration, Grad–Rubin iteration, MHD relaxation, the optimization approach, and so on (see a review by Wiegelmann & Sakurai 2021). The computation speed and accuracy of different numerical methods can vary significantly given the differences in algorithms and their specific realizations in many aspects. We apply a kind of MHD relaxation method with a conservation element/solution element (CESE) solver (Jiang et al. 2011). The so-called CESE-MHD-NLFFF code (Jiang & Feng 2013) has been tested by different benchmark cases (Low & Lou 1990; van Ballegooijen & Mackay 2007; Metcalf et al. 2008). And it has also been widely applied to the magnetic field extrapolation of realistic solar magnetic field data (Jiang & Feng 2013; Jiang et al. 2014; Duan et al. 2017, 2019). As these numerical extrapolation results have gone through a series of quality checks by different kinds of metrics and have shown good agreement between extrapolated field lines and observational features like sigmoids, coronal loops, and even an elongated quiescent filament, it is practical and promising to use this method to contribute to the quantitative study of CME-MFRs. In addition, we will combine the in situ spacecraft measurements of the interplanetary counterpart to help with the interpretation and validation of our analysis results.

Understanding toward the formation and evolution process of CME-MFRs will ultimately help us make a definitive and physical connection between the origin of solar MFRs (including the MFRs before and after the eruption) and their interplanetary counterparts. Such a connection can be pursued through a quantitative study of MFRs' physical characteristics (e.g., magnetic flux, field line twist, and electric current). Specifically, one critical step is the detailed analysis of available solar observations in order to determine whether an MFR exists or how one can form prior to and during the eruption. Characterization of MFR properties not only plays a major role in understanding the physical mechanisms underlying solar eruption and the subsequent evolution, but also contributes to the improvement of forecast ability in space weather.

Table 1
Timelines of Two Flare–CME–ICME Events Observed by Multiple Spacecraft (All Times Are in UT)

Flare Peak Time	Magnitude	Location	STEREO CME Time	SOHO/LASCO CME Time	Wind/ICME Arrival Time
2013-04-11T07:16	M6.5	N07E13	07:39	07:24	04-14T17:00
2014-09-10T17:45	X1.6	N11E05	17:54	18:00	09-12T22:00

In this paper, we carry out coronal magnetic field extrapolation based on the method developed by Jiang & Feng (2013) for two events to obtain the 3D magnetic field topology of the AR prior to eruption. In addition to the magnetic field extrapolation, we estimate the possible locations of the MFR's footpoints prior to eruption and measure a number of magnetic field parameters (including the magnetic reconnection flux derived from the flare ribbons) in the corresponding AR during the eruption process from different observations. Then the results from extrapolation and observation are combined to identify whether there is a coherent preexisting MFR before the eruption and to interpret how such a structure may evolve during and following the corresponding flare and CME eruption process. The magnetic properties of the CME-MFR will be further analyzed and compared with in situ ICME/MC modeling results, which are obtained separately.

This article is organized as follows. The two selected events and extrapolation method are introduced in Section 1. Then we describe the identification methods and analyze results associated with the MFRs on the Sun in Section 2. The magnetic properties of the MFRs are estimated quantitatively and presented in Section 3 based on results from both the solar source region and in situ modeling. The conclusion is given in Section 4.

2. Event Selection and Extrapolation Method

2.1. Event Overview

For the purpose of performing a quantitative study of CME-MFRs, we search for appropriate event candidates from a list of reconstructed MFRs based on photospheric magnetograms before eruption by Duan et al. (2019). They extrapolated the 3D magnetic field in ARs for 45 major flare eruption events employing the NLFFF extrapolation code by Jiang & Feng (2013). With a set of criteria similar to those by Jing et al. (2018), all major flares that are above GOES class M5 and occurred within 45° of the solar disk center from 2011 January to 2017 December are selected. Moreover, we examine the associations between flare and CME, and between CME and ICME to ensure that there exists a well-established one-to-one connection between a flare, an associated CME, and an ICME based on the work by Zhu et al. (2020). Two events are selected for this study as shown in Table 1. Both ARs related to the two events are located near the disk center. The CMEs associated with the corresponding flares in these two events have been both observed by the SOHO and STEREO spacecraft close to the peak times of the corresponding flares (Vemareddy & Zhang 2014; Cheng et al. 2015; Cheng & Ding 2016; Joshi et al. 2017). And the associated ICME/MC events were also observed by the Wind and ACE spacecraft at 1 au, which have been reported by Hu et al. (2021a) and Kilpua et al. (2021), respectively.

In event 1, an M6.5 flare was produced at ~6:55 UT on 2013 April 11 (N07E13). Then a halo CME appeared in the field of view of SOHO/LASCO after 07:24 UT, and the same CME was also observed simultaneously by both STEREO A and B spacecraft after ~07:39 UT. The corresponding ICME/MC passing Earth was detected about 3 days later (Hu et al. 2021a). Similar examination is conducted for the second event, which started with an X1.6 flare peaking at ~17:45 UT on 2014 September 10 (N11E05). There was also a halo CME following the flare based on the observations from SOHO/LASCO and the coronagraph of STEREO B (data from STEREO A is unavailable for event 2). After 2 days, the Wind spacecraft encountered the subsequent ICME/MC structure at Earth (Kilpua et al. 2021). Therefore, the connections of CME-MFRs from the Sun to the Earth are well established for these two events. We will mainly present a quantitative study of the CME-MFR before eruption hereafter.

2.2. CESE-MHD-NLFFF Extrapolation Method

The CESE-MHD-NLFFF code solves the MHD momentum equation and the magnetic induction equation iteratively until a stationary magnetic field solution is reached, similar to a magnetofrictional approach. As a special case of the MHD relaxation method, the magnetofrictional method includes an artificial dissipative term $\boldsymbol{D}(\boldsymbol{v})$ to balance the momentum equation with flow velocity $\mathbf{v}$. Specifically, in the CESE-MHD-NLFFF code, $\boldsymbol{D}(\boldsymbol{v})$ is written in a frictional form $\nu\rho\boldsymbol{v}$ (see below, and Jiang & Feng 2012) along with some modifications in order to utilize the existing CESE-MHD solver. The modified momentum equation and the induction equation are written as (Jiang & Feng 2012, 2013)

$$\frac{\partial(\rho\boldsymbol{v})}{\partial t} = (\nabla \times \boldsymbol{B}) \times \boldsymbol{B} - \nu\rho\boldsymbol{v},\ \rho = |\boldsymbol{B}|^2 + \rho_0. \quad (1)$$

$$\frac{\partial \boldsymbol{B}}{\partial t} = \nabla \times (\boldsymbol{v} \times \boldsymbol{B}) - \boldsymbol{v}\nabla \cdot \boldsymbol{B} + \nabla(\mu\nabla \cdot \boldsymbol{B}). \quad (2)$$

Here the (pseudo) mass density ρ also contains a constant ρ_0 for simplicity and is assumed to be largely proportional to $|\boldsymbol{B}|^2$ in order to roughly equalize the speed of the evolution of the entire field with nearly uniform Alfvén speed ($v_A = \frac{|\boldsymbol{B}|}{\sqrt{\rho}} \approx$ const). To enhance the ability of handling noisy data in realistic solar magnetograms, a small value ρ_0 is added, e.g., $\rho_0 = 0.1$ (in the same unit as $|\boldsymbol{B}|^2$), to the original pseudo density ρ. Two extra terms are added to control the divergence of the magnetic field in the induction equation. More details can be found in Jiang & Feng (2012, 2013).

2.3. Data Preprocessing and Grid Initialization

Passing across the inhomogeneous plasma environment, the plasma β could vary from $\beta > 1$ in the photosphere to $\beta \ll 1$ in the low and middle corona, and to $\beta > 1$ again in the upper corona (Gary 1989, 2001). So the force-free condition may not be always satisfied especially at the photosphere (Metcalf et al. 1995). One way to get a more consistent boundary condition for NLFFF extrapolation is to modify the raw photospheric magnetogram so it

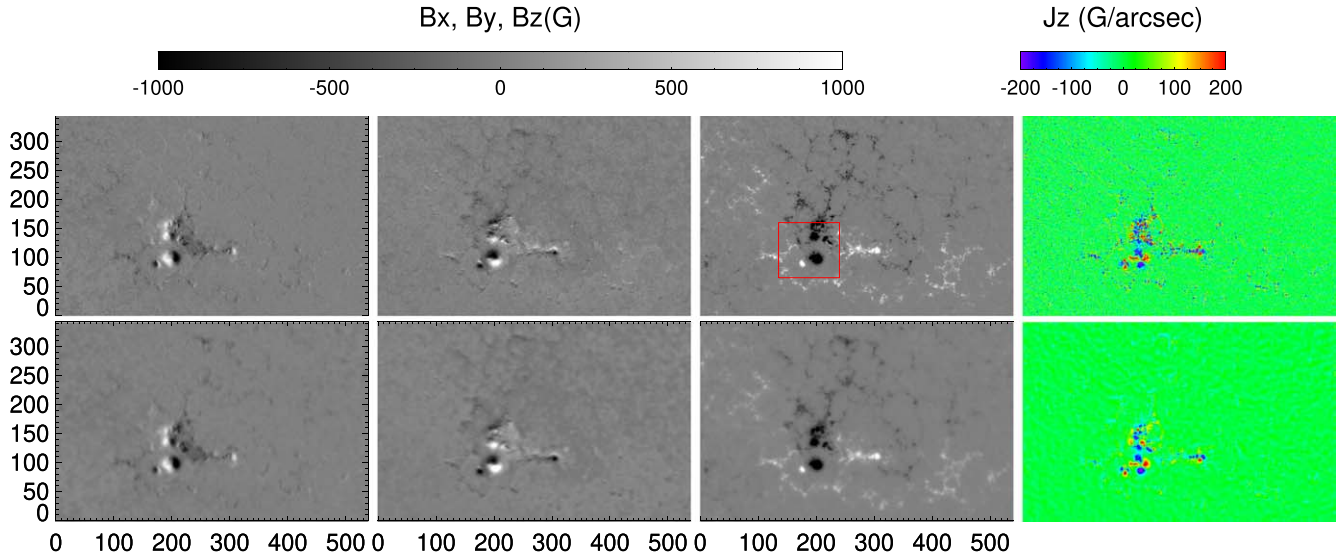

Figure 1. First row (from the left to the right panels): The three components B_x, B_y, and B_z of the raw magnetogram and the derived vertical current density J_z distribution for event 1, AR 11719, at 06:36 UT on 2013 April 11. The red box marks the bottom side of a subvolume. Second row: The corresponding maps from the preprocessed magnetogram. The size of each map is $540'' \times 344''$.

mimics a force-free chromospheric magnetogram, by so-called preprocessing, which was first proposed by Wiegelmann et al. (2006). We use the preprocessing code developed by Jiang & Feng (2014), which is made consistent with the CESE-MHD-NLFFF extrapolation code by adopting an optimal magnetic field splitting form. Such a procedure is designed to improve the quality of the raw magnetogram to make it closer to the force-free condition and smooth the raw data to help reduce measurement uncertainties and numerical errors from the computation.

High-resolution vector magnetograms are routinely observed by SDO/Helioseismic and Magnetic Imager (HMI; Schou et al. 2012). Specifically, the Space-weather HMI Active Region Patch (SHARP; Bobra et al. 2014) vector magnetogram data product `hmi.sharp_cea_720s`, provided by SDO/HMI, is used as the input for the extrapolation. The SHARP data series provide maps following each patch of significant solar magnetic field for its entire lifetime and the data is also derotated to the disk center and remapped using the cylindrical equal-area Cartesian coordinates. Photospheric vector magnetograms are included with a cadence of 720 s and a spatial resolution of $0\farcs5$ (~0.36 Mm). For the two selected events, vector magnetograms from the ARs at least 10 minutes before the flare onset times (estimated from the soft X-ray measurement of GOES) are preprocessed to get the necessary boundary conditions and derive the initial conditions from a potential field solver for the NLFFF extrapolations. The original magnetograms are rebinned from $0\farcs5$ per pixel to $1''$ per pixel for the preprocessing procedure and the subsequent extrapolations. The overall smoothing effect is presented in Figures 1 and 2 as a result of preprocessing for the two events by comparing the raw and preprocessed maps of magnetograms and current density J_z distributions. Random noise is obviously suppressed in the J_z maps. The unsigned vertical flux in the z direction of AR 11719 in Figure 1 is about 1.556×10^{22} Mx, and that of AR 12158 in Figure 2 is about 2.386×10^{22} Mx. The ratios of the total net magnetic flux to the total unsigned flux are about 0.0747 and 0.0752 for the two events, respectively. The CESE-MHD-NLFFF code does not require exact flux balance on the bottom boundary.

For consideration of the speed and accuracy of the computation in terms of high-resolution and large-field-of-view solar magnetograms, a nonuniform grid structure within a block-structured parallel computation framework is adopted with the help of the PARAMESH software package (MacNeice et al. 2000) for the CESE-MHD-NLFFF code. For the grid initialization, the whole computation domain includes the preset main computation region and the surrounding buffer zones to reduce the influence of the side boundaries (Jiang & Feng 2013) since the magnetic fields at these numerical boundaries are simply fixed to their initial values (i.e., those of the potential field). Then the whole computational domain is divided into blocks with different spatial resolutions and all blocks have identical logical structures that are evenly distributed among processors. As we vary the grid size only in height (the z dimension) for this study, the grid resolution matches the resolution of the magnetogram at the bottom boundary and decreases by four times at the top of the computational domain. After the grid initialization, the initial condition of the whole computation domain is assigned by a potential field solution derived from the input magnetogram by using the Green's function method (Chiu & Hilton 1977; Metcalf et al. 2008).

2.4. Convergence Study and Extrapolation Metrics

Before we start our analysis for the two events, we also examine the relaxation process by several metrics to obtain converged extrapolation results. These include the residual of the field between two successive iteration steps, the force-freeness of the numerical result *CWsin*, the divergence-free condition $\langle |f_i| \rangle$ (Wheatland et al. 2000; Metcalf et al. 2008), and the total magnetic energy $E_{\rm tot}$ (see their definitions in the Appendix).

For event 1, we carry out the extrapolation based on the whole SHARP vector magnetogram ($540'' \times 344''$) and then calculate the convergence metrics for every 200 iteration steps as shown in the first column of Figure 3 with the finest grid size $1''$. As shown in Figure 3, the residual goes through a gradual increase before ~6500 iteration steps because the bottom boundary condition drives the system away from the initial potential field (Jiang & Feng 2012). Even though obvious fluctuations appear after the initial driving process, the overall

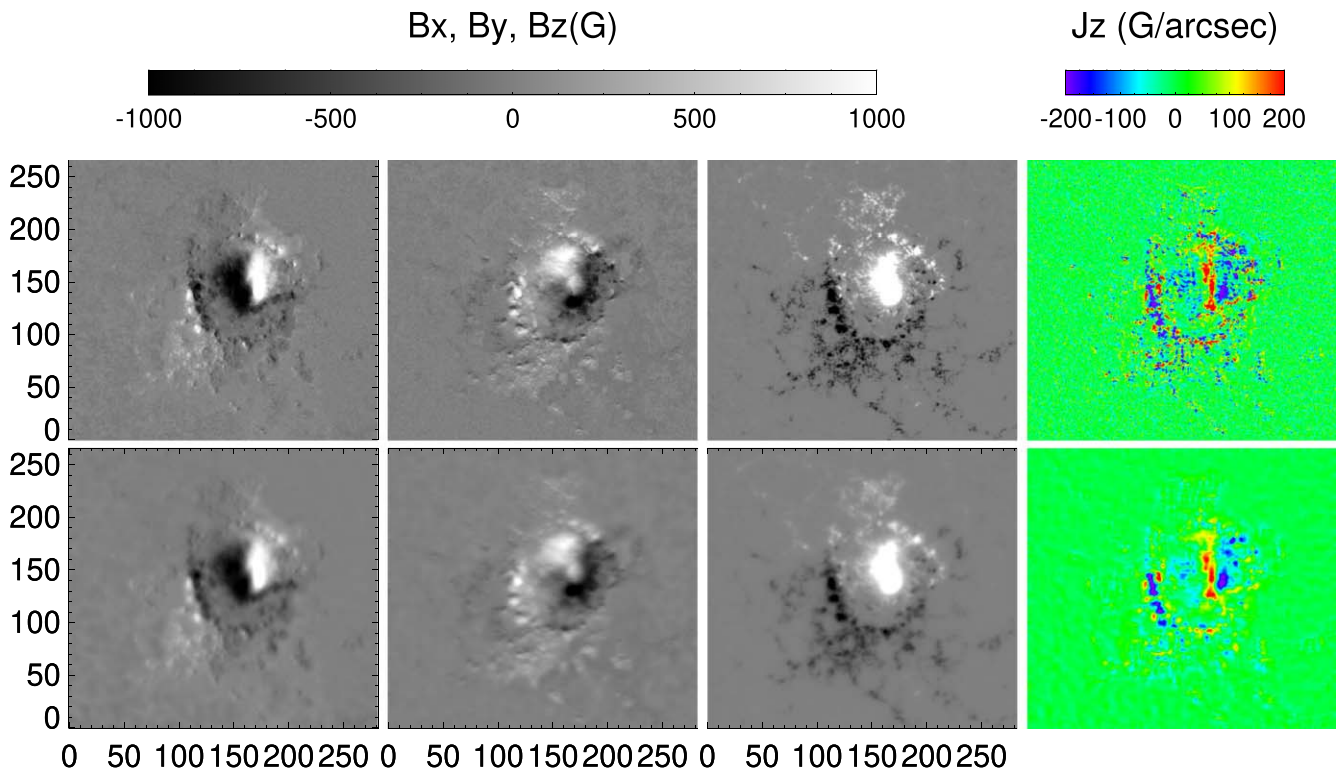

Figure 2. The raw and preprocessed maps for event 2, AR 12158, at 17:00 UT on 2014 September 10. The format is the same as that of Figure 1. The size of each map is $282'' \times 266''$.

trend of the residual toward the end is decreasing, accompanied by small oscillations. After ~30,000 iteration steps, the residual is reduced to $\sim 10^{-5}$ and maintains a declining trend. Other metrics also display a trend with little variation and both *CWsin* and $\langle |f_i| \rangle$ reach relatively small values. Thus this extrapolation result can be considered as a converged solution. It is noticed that there are some oscillations in the convergence process, which may be caused by the broad distribution of the weak field and random noise from the input magnetogram. The total computation time (to convergence until 40,000 iteration steps) is about 95 hr with 19 cores on a 24-core local desktop with 48 GB memory.

For event 2, the size of the SHARP magnetogram is $282'' \times 266''$. One run is carried out with the smallest grid size $1''$ and the full-size magnetogram. The second column of Figure 3 shows a smooth convergence process. The residual converges very fast after an initial rise exceeding 10^{-4} to an order-of-magnitude smaller value, $<10^{-5}$, within 11,000 iterations. All the other metrics show clear monotonic decreases and stabilize after ~11,000 iterations, which is consistent with the optimal convergence pattern in previous tests of this code (Jiang & Feng 2012; Jiang et al. 2012; Jiang & Feng 2013). This convergence process is relatively smooth without any spurious oscillations, so a final solution with good indication of convergence is readily obtained for subsequent analysis. It takes about 23 hr with 19 cores on the same local desktop for the extrapolation result to converge (after 20,000 iteration steps).

To further check the quality of force-freeness and divergence-freeness of the converged extrapolation results, calculations of metrics like *CWsin* and $\langle |f_i| \rangle$ for the two events are also shown in Table 2. The *CWsin* values for the two ARs are around 0.3–0.5, which are much larger than the values obtained from previous tests for ideal benchmark solutions (which are less than 0.1; Jiang & Feng 2013) but are similar to many other reported NLFFF extrapolation results for realistic magnetograms. The typical range for *CWsin* is 0.1 to 0.5 (see, e.g., De Rosa et al. 2009; Jiang & Feng 2013). It should also be noted that although $CWsin \ll 1$ indicates a force-free field, a large *CWsin* value does not mean the opposite (Jiang et al. 2012), considering that this is one weighted average over the whole computational domain. In the current-free region, $\boldsymbol{J} = \nabla \times \boldsymbol{B}$ may be nonzero due to the numerical finite differences. In addition, small-scale structures in the magnetograms (where the magnetic field strength is usually low) may increase the *CWsin* value as the derived currents might not be low and have random orientations. Here we add two additional metrics $E_{\nabla \times \boldsymbol{B}}$ and $E_{\nabla \cdot \boldsymbol{B}}$ to evaluate the force-freeness and divergence-freeness by analyzing the residual force for a chosen volume (see descriptions in the Appendix). Considering the broad distribution of the weak field in event 1, the metrics for a subvolume with a strong magnetic field as marked by the red box in Figure 1 are also derived. All the metrics are very close to the previously reported results for the CESE-MHD-NLFFF extrapolation of different ARs (Jiang & Feng 2013; Duan et al. 2017).

3. Characterization of MFRs on the Sun

3.1. MFR Identification Method

Both extrapolation and observation results are critical for MFR identification on the Sun. As for the observational analysis of MFRs, we analyze the data from the Atmospheric Imaging Assembly (AIA; Lemen et al. 2012) and HMI on board the SDO spacecraft to study the evolution of the corresponding flares for the two events. SDO/AIA provides full-disk images in seven EUV and two UV wavelength channels with a high spatial

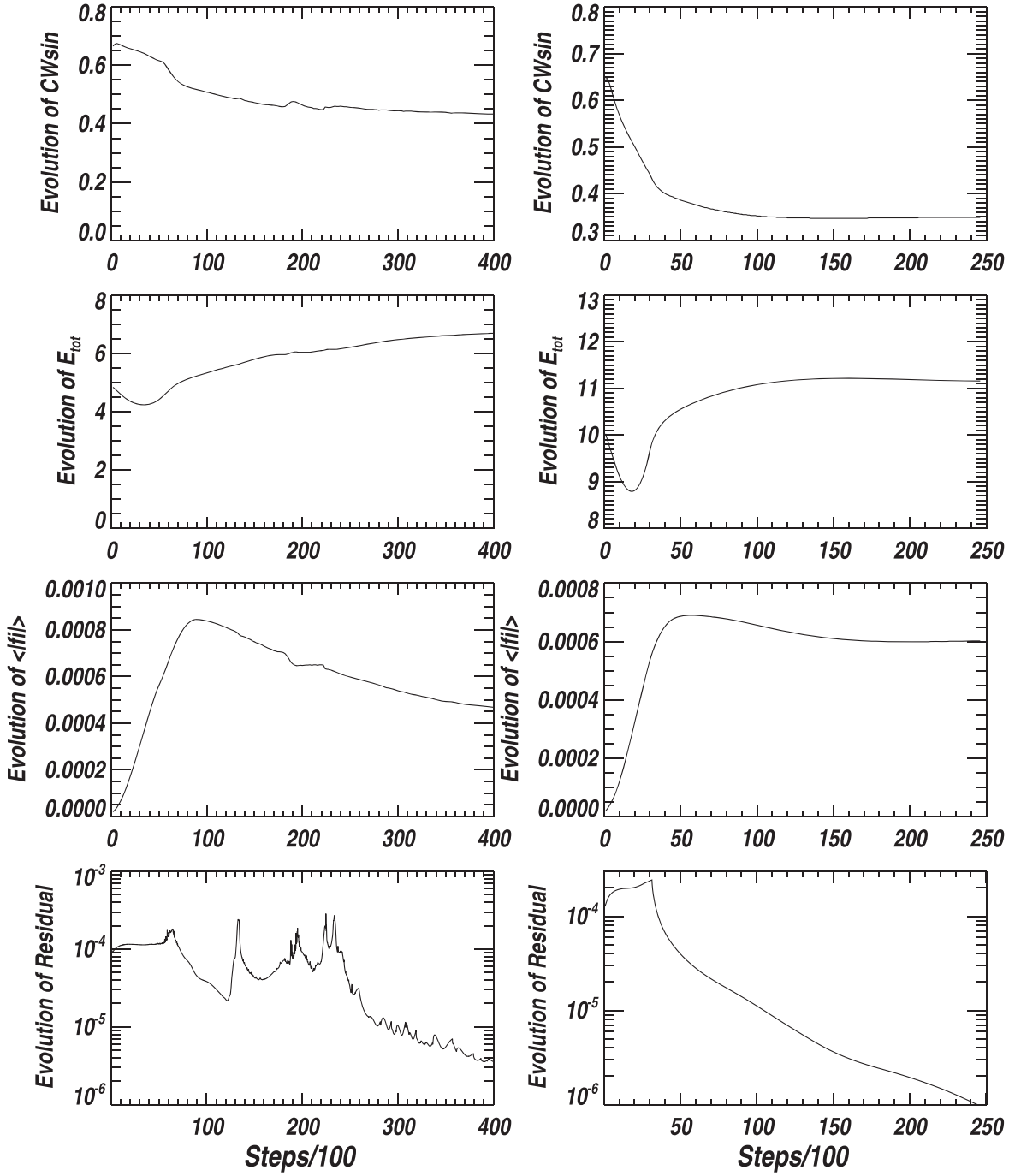

Figure 3. Two sets of convergence metrics for two extrapolation runs for AR 11719 (event 1, left column) and AR 12158 (event 2, right column). The top three rows show the metrics of *CWsin*, total magnetic energy $E_{\rm tot}$ (arbitrary units), and $\langle|f_i|\rangle$, respectively. Panels in the bottom row show the evolution of residuals for the two events.

Table 2
NLFFF Extrapolation Metrics of Force-freeness and Divergence-freeness for Two ARs

AR	*CWsin*	$\langle\lvert f_i\rvert\rangle$	$E_{\nabla\times\boldsymbol{B}}$	$E_{\nabla\cdot\boldsymbol{B}}$
AR 11719 Full Volume	0.449	2.59×10^{-4}	0.195	3.38×10^{-2}
AR 11719 Subvolume	0.384	4.56×10^{-4}	0.177	2.61×10^{-2}
AR 12158 Full Volume	0.368	3.81×10^{-4}	0.161	4.05×10^{-2}

resolution (0.″6 per pixel and a total of 4096×4096 pixels per image) and a moderate time cadence (12 s in the EUV channels and 24 s in the UV channels).

To provide additional support for MFR identification and characterization of the corresponding CME-MFRs at a different stage besides the extrapolation, we also analyze the evolution of the flare ribbons and the corresponding magnetic reconnection properties. Flare ribbons map the footpoints of reconnected field lines. Magnetic reconnection beneath the erupting MFR forms flare loops, and the same amount of reconnected magnetic flux is injected into the MFR. Reconnection may also take place between the erupting MFR and the ambient magnetic field, although this is not the main focus of this study. Therefore, magnetic reconnection flux associated with flare

ribbons is useful to establishing a quantitative connection between MFRs on the Sun (both before and after the flare eruption) and their interplanetary counterparts. The amount of accumulative magnetic reconnection flux can be measured by summing the magnetic flux in newly brightened UV pixels within flare ribbons. In this study, we employ 1600 Å data from SDO/AIA and vector magnetograms from SDO/HMI to measure the magnetic reconnection flux and magnetic reconnection rate from brightening pixels, following the automated approach developed by Qiu et al. (2002, 2004). The brightening ribbon pixels are chosen when the intensity of the pixel is greater than four, five, or six times the median intensity, which is fixed and determined from the average of a 6 minute time period (for a region of interest before the eruption). These threshold values are used to distinguish flare brightening from plage emission. A flare ribbon pixel also should stay bright for at least 4 minutes, which helps minimize effects due to saturation or projection of bright coronal ejecta. The reconnection flux quoted in Table 4 is the average of the measurements using these three thresholds and in the positive and negative magnetic fields, and the standard deviation of these measurements is quoted as the measurement uncertainty. A discussion of the measurement method and uncertainties is given in Qiu et al. (2007, 2010).

While an MFR is generally considered as a group of coherent winding field lines with both ends rooted on the photosphere before eruption, it has not been quantitatively defined in a universal way. Identifying a coherent MFR based on a reconstructed coronal magnetic field derived from a real magnetogram can be difficult, given the complex magnetic topology. Liu et al. (2016) suggested that the magnetic twist number T_w can serve as a good proxy for finding the axis of an MFR. The twist number T_w measures how many turns two infinitesimally close field lines wind about each other in (see Berger & Prior 2006), and is defined by

$$T_w = \int_L \frac{\mu_0 J_{\parallel}}{4\pi B}\, dl = \frac{1}{4\pi}\int_L \frac{(\nabla \times \boldsymbol{B})\cdot \boldsymbol{B}}{B^2}\, dl,$$
$$= \frac{1}{4\pi}\int_L \alpha\, dl, \text{ if} \nabla \times \boldsymbol{B} = \alpha \boldsymbol{B}. \quad (3)$$

Here α is the force-free parameter and the integral is taken along one magnetic field line with path length L, starting from one end point of the field line on the boundary to the other. For both events, extrapolation results are generated utilizing magnetograms that are chosen at least 10 minutes before the flare onset times. We calculate the twist number T_w at each grid point in the whole volume with the same grid size as the resolution of the input magnetogram, i.e., 1″. Then we start the topology analysis with the definition of Liu et al. (2016) that an MFR has a bundle of field lines spiraling around the same axis or each other by more than one turn ($|T_w| \geqslant 1$; see also Duan et al. 2019). Combined with the field line topology, one may also require that such a constrained MFR volume be a single tube without multiple bifurcations. However in reality, such bifurcations are common, which often indicate that the pair of identified footpoint regions with positive and negative polarities may not contain the same amount of magnetic flux. In other words, the field lines originating from the positive-polarity region may not all end in the corresponding conjugate negative-polarity region. In addition, the footpoints of MFRs should be restricted within or close to the main flare ribbon areas identified from AIA observations, given the general relation between the magnetic reconnection process during flares and the formation of erupting CME-MFRs (Moore et al. 2001; Qiu et al. 2004; Qiu 2009; Zhu et al. 2020).

3.2. Results for AR 11719

For event 1 in AR 11719, simultaneous observations of the flare's time evolution in the SDO/AIA 94, 131, and 1600 Å wavelength channels before and during the flare eruption are given in Figure 4. From the EUV observations in 94 Å and 131 Å, some curved structures are present near the center before the flare eruption, which were recognized as hot channels in Cheng & Ding (2016). But such a sigmoid-like structure based on emission line images does not necessarily yield a similarly continuous magnetic field line configuration (Titov & Démoulin 1999; Schmieder et al. 2015; Cheng & Ding 2016; Duan et al. 2017), i.e., that of an MFR. Instead, these brightened features may correspond to groups of short sheared arcades that are discontinuous, based on the extrapolation result to be demonstrated below. In the bottom panels of Figure 4 for the 1600 Å UV observation, there is a typical flare morphology with two brightening ribbons lying nearly in parallel with each other, expanding, and then drifting away from each other during the time evolution. The contours of the flare ribbons coincide with the curved brightening structures in the 131 Å observation at the central region, especially toward the "hooked" ends, which gives us a rough estimation of possible positions for the MFR footpoints for this event.

The time evolution of the flare ribbons in the corresponding SDO/HMI magnetograms, which are remapped to the subareas in SDO/AIA's field of view, is shown in Figure 5, in the left column. Besides that, we add the X-ray flux measurement of the whole Sun provided by GOES for wavelengths of soft X-ray (1–8 Å) during the same time period in the right column, together with concurrent measurements of the accumulative magnetic reconnection flux and magnetic reconnection rate by the approach of Qiu et al. (2002). This M6.5 flare eruption starts at ~06:55 UT according to the rapid change of the soft X-ray flux curve, which is consistent with the onset of the magnetic reconnection flux increase shown in the second panel in the right column. Based on the average of the total unsigned magnetic flux in each enclosed ribbon area with one dominant polarity (either positive or negative; Kazachenko et al. 2017), the final accumulative magnetic reconnection flux reaches a magnitude of $17 \pm 2.8 \times 10^{20}$ Mx after the eruption. Given the association between the magnetic reconnection flux and the flux content of the corresponding ICME/MC flux ropes (e.g., Qiu et al. 2007; Hu et al. 2014), such flux measurement from flare ribbons can be helpful in making further connections between MFRs on the Sun and their in situ counterparts, as laid out in Section 4.

In Figure 6(a), some sample field lines are drawn over the corresponding AIA 94 Å image to give a qualitative comparison between the extrapolation result and the observation. Several loop structures are recovered overlapping with selected field lines, and a set of twisted field lines lying around the PIL takes a shape resembling the middle of the inverse "S" sigmoid seen in the 94 Å channel (see also Figure 6(c)). Among the comparisons with the 1600 Å observation in Figure 6(b), the footpoints of the twisted field lines located close to the flare ribbons are associated with grid points with negative T_w values.

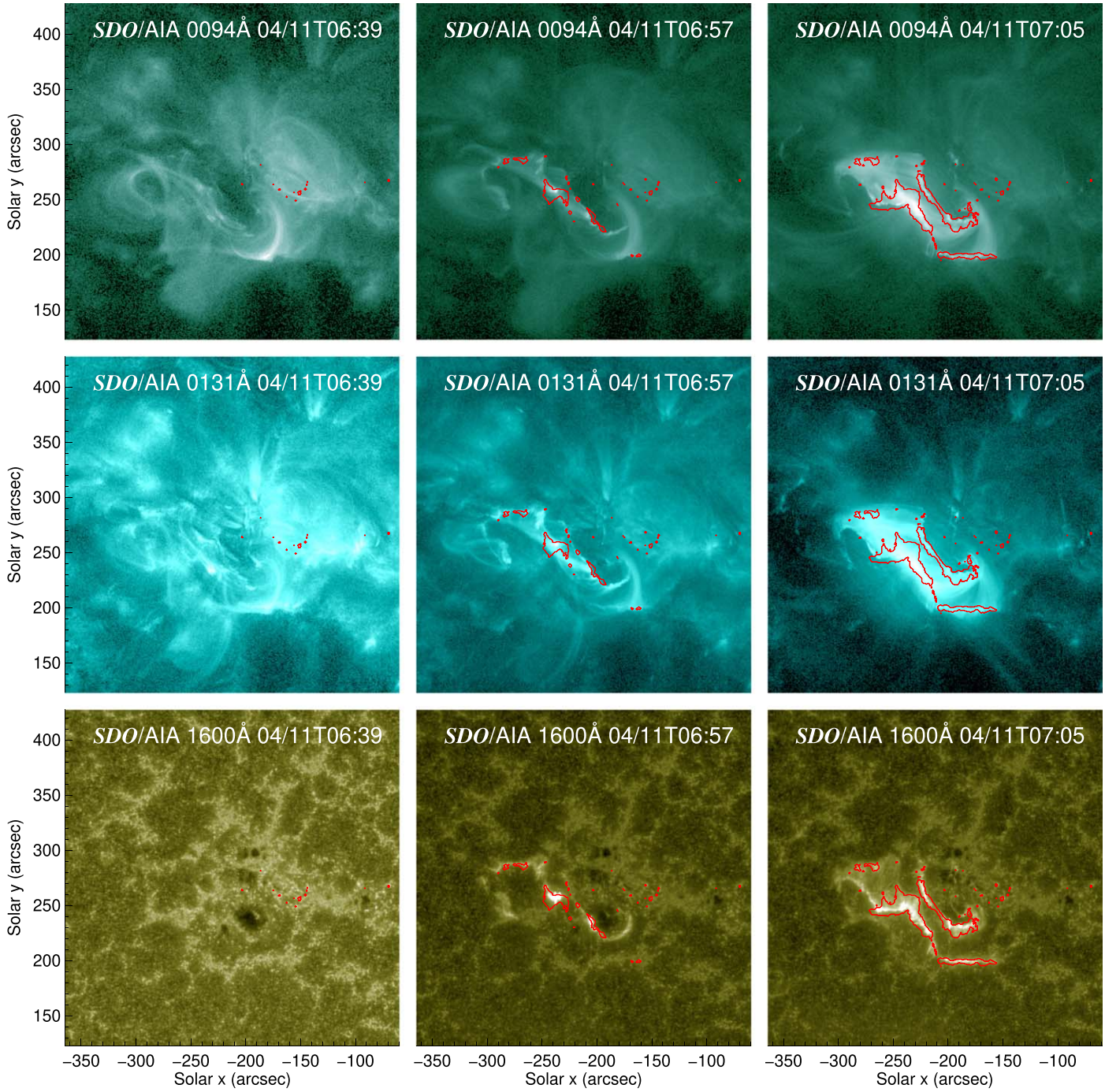

Figure 4. Observations from SDO/AIA in 94 Å, 131 Å, and 1600 Å (from top to bottom row) wavelength channels at three different times as marked in each panel (from left to right) of AR 11719 for event 1. The contours of the flare ribbons in red as observed in 1600 Å are also overlaid on the 94 Å and 131 Å plots, which are observed at the same times.

On a plane near the bottom layer (at $z = 2''$ above the photosphere), we pick all points with $T_w \leqslant -1$ around the central sigmoidal structure, and plot field lines passing through this set of seed points. We eliminate open field lines, which only have one end point attached to the bottom boundary and are thus not "closed," and also ill-defined T_w values. As a result, as shown in Figure 6(b), four groups of field lines are distinguished starting with the selected seed points. Compared to the locations of the flare ribbons, three groups of field lines are excluded since a part of their footpoints extends out of the ribbon sites. Therefore the remaining bundle of field lines shown in Figure 6(c) is identified to be the most likely MFR candidate for the 2013 April 11 event before the flare eruption. After determining the MFR, we can find the axial field line with the maximum $|T_w|$ of the MFR. The axis of the identified MFR in event 1 possesses $T_w = -1.5$, which lies close to the bottom boundary and reaches a maximum height of $z \sim 19''$. The time sequence of flare ribbons after 6:42 UT is then coaligned with the bottom boundary magnetogram and overplotted in the usual way, color-coded by elapsed time, in Figure 6(d). It shows that two groups of identified MFR footpoints are located on opposite sides of the flare ribbons near the far ends, consistent

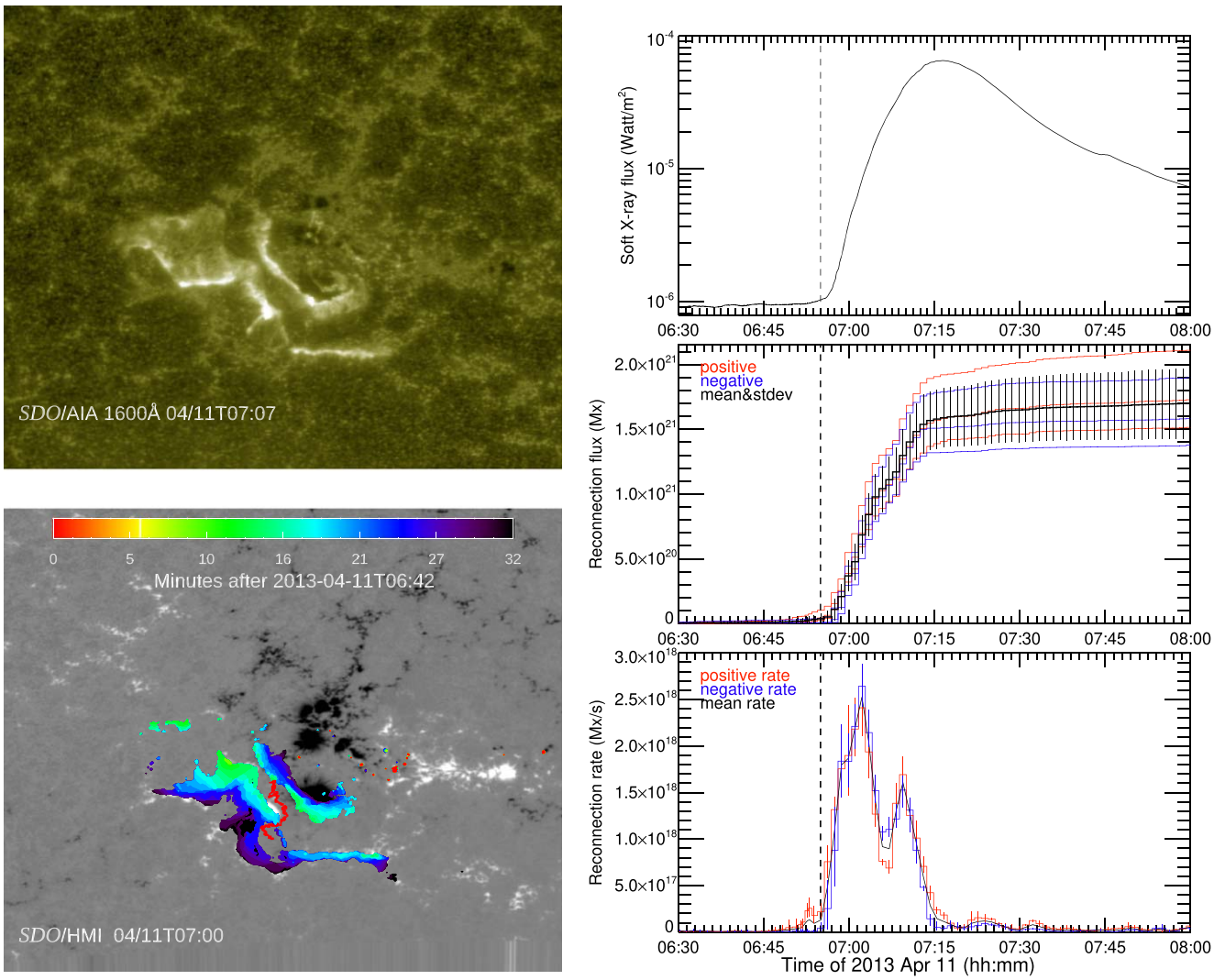

Figure 5. Left column: observation of flare ribbons in 1600 Å passband (top panel) and the time evolution of the flare ribbons overplotted on the coaligned HMI magnetogram for event 1 (bottom panel), where the areas swept by the flare ribbons are colored by the elapsed time in minutes as denoted by the colorbar. The thick red curve lying in the middle of the lower panel marks the PIL. Right column: GOES soft X-ray (1–8 Å) flux measurement for the flare in event 1 (top panel); the magnetic reconnection flux measured from 1600 Å observation (middle panel) for both positive (red) and negative (blue) flux measurements with uncertainty limits based on different background removal criteria, and the unsigned mean flux, which is shown in black with the standard deviation represented by the error bars; and the corresponding magnetic reconnection rates for event 1 (bottom panel). The dashed lines in all three panels indicate the flare onset time of event 1.

with the scenario proposed by Moore et al. (2001). If the MFR is strictly confined to be the field lines shown here with two and only two opposite-polarity ends all rooted on the photosphere, then its footpoints are just part of the regions identified based on the $|T_w|$ threshold conditions we describe earlier in Section 3.1.

To further confirm the existence of the MFR, we also check different topological properties from a side view. The coherent MFR structure is maintained with a different $|T_w|$ threshold as seen in Figures 7(a) and (b). The distribution of the quantity $|\boldsymbol{J}|/|\boldsymbol{B}|$ as a proxy for current density is displayed in Figures 7(c) and (d) on a cross-section plane nearly perpendicular to the MFR. The current density $|\boldsymbol{J}|$ itself shows a similar distribution. Based on the current density distribution at the intersections between the identified MFR field lines and the vertical slice in Figure 7(c), the flux rope goes through a region with relatively high current density. The geometric boundary of an MFR can also be estimated by the location of a quasi-separatrix layer, a very thin layer where there is a strong gradient of field line connectivity (Demoulin et al. 1996). Such a feature is typically defined mathematically by a high squashing factor Q (Titov et al. 2002; Vemareddy 2021). As shown in Figures 7(e) and (f), the identified group of field lines with small Q values is surrounded indeed by a clear boundary with a high squashing degree Q.

3.3. Results for AR 12158

Observations of the flare ribbon evolution before and during the flare eruption for event 2 in AR 12158 are shown in Figure 8. Event 2 also exhibits a two-ribbon flare morphology, with the two ribbon areas colocated near the two ends of an inverse "S" shaped sigmoidal structure. The southward ribbon has a more dominant swept area in terms of size than the other. Similarly, we use the overlapping regions between the flare ribbon areas and the curved brightening sigmoidal structures in the 131 Å observation to approximate the possible locations of MFR footpoints in this event.

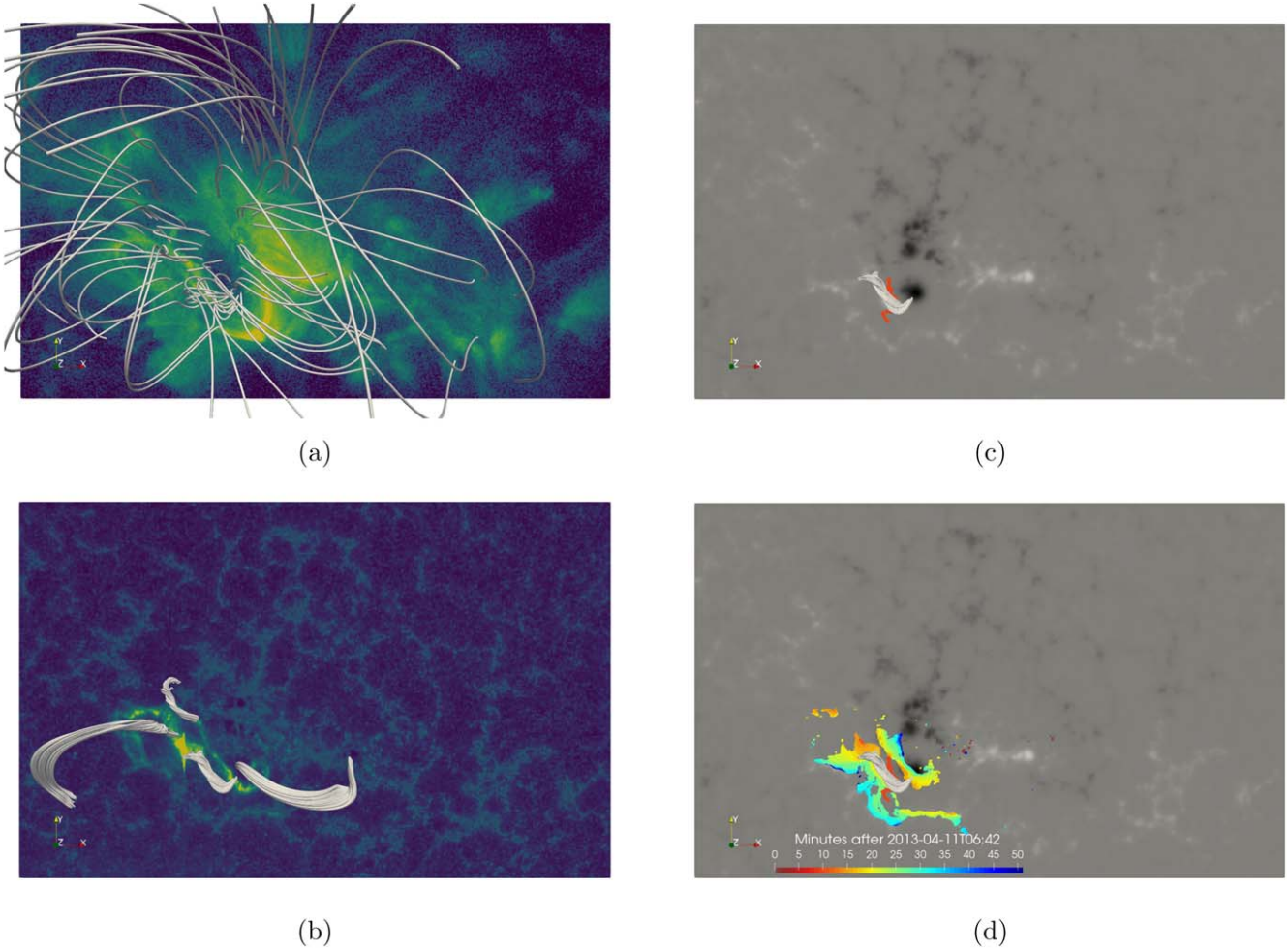

Figure 6. Identification of an MFR for event 1: (a) the overall field line configuration superimposed on an AIA 94 Å image observed at 06:36 UT, (b) field line groups identified from the extrapolation result based on the criterion of $|T_w| > 1$ overplotted on an AIA 1600 Å image observed at 06:59 UT, (c) the field lines of the identified MFR, and the underlying PIL in red drawn over the corresponding line-of-sight HMI magnetogram, and (d) the same as (c) except for the additional superimposed flare ribbons, which are color-coded by elapsed time in the same way as in Figure 5.

In Figure 9, we show the same set of panels for event 2, as in Figure 5. We find that the initial enhancement of the X-ray flux is earlier than the significant increase of the magnetic reconnection flux. After a slow rise phase with a low reconnection rate, a strong flare is produced quickly after ~17:20 UT. The final accumulative magnetic reconnection flux reaches a magnitude of $47 \pm 7.5 \times 10^{20}$ Mx for event 2. The flare ribbon morphology still exhibits general features for a "two-ribbon" flare, although the asymmetry of the spatial distributions is more pronounced, indicating perhaps a more significant deviation from the "standard" 2D geometry.

For event 2, the configuration of magnetic field lines from the extrapolation result has a good visual correspondence with the AIA observations as shown in Figures 10(a) and (b). There is a clear inverse "S" sigmoid structure near the center imaged by the AIA 94 Å passband. However, the core field in our extrapolation result mainly consists of several groups of sheared arcade structures overarched by higher coronal loops, rather than one continuous inverse "S" structure (see also Duan et al. 2017). Based on the long-term evolution before the eruption, Cheng et al. (2015) found that there is a central sigmoid structure initially appearing in the AIA 94 Å passband at ~15:10 UT and then it goes through repetitive disappearance and reappearance processes. So they suggested that a nascent MFR is under formation prior to the major eruption by tether-cutting reconnection. After ~16:55 UT, the sigmoid develops quickly and produces an X1.6 flare and a CME. In order to find a possible MFR structure prior to the flare, we take a look at the T_w distribution and find that the majority of the core field region has a negative and relatively small twist number such that $|T_w| < 1$. This indicates the absence of a twisted coherent MFR according to the criterion we are using (Liu et al. 2016; Duan et al. 2019). In Figures 10(c) and (d), we show the isosurfaces of $T_w = -1$ and $T_w = -0.8$ in the central volume. There is no coherent structure under the $T_w = -1$ criterion, though several coherent structures appear for a lower threshold in magnitude $T_w = -0.8$. Comparing these field line bundles with the locations of the flare ribbons, there are two coherent weakly twisted field line groups as presented in Figure 10(e). The left group has a maximum $|T_w| \sim 0.82$ but extends to a relatively faraway location from the ribbon (and also to a height of $z \sim 50''$). It also appears to be nearly perpendicular to the local PIL. Another group of field lines lies close to the bottom boundary and has a maximum $|T_w| \sim 0.97$, which still, strictly speaking, fails to satisfy the MFR criterion. In addition, the current density distribution in Figure 10(f) at the intersections of a vertical slice with the two field line bundles shows less clearly defined concentrations in those field line regions.

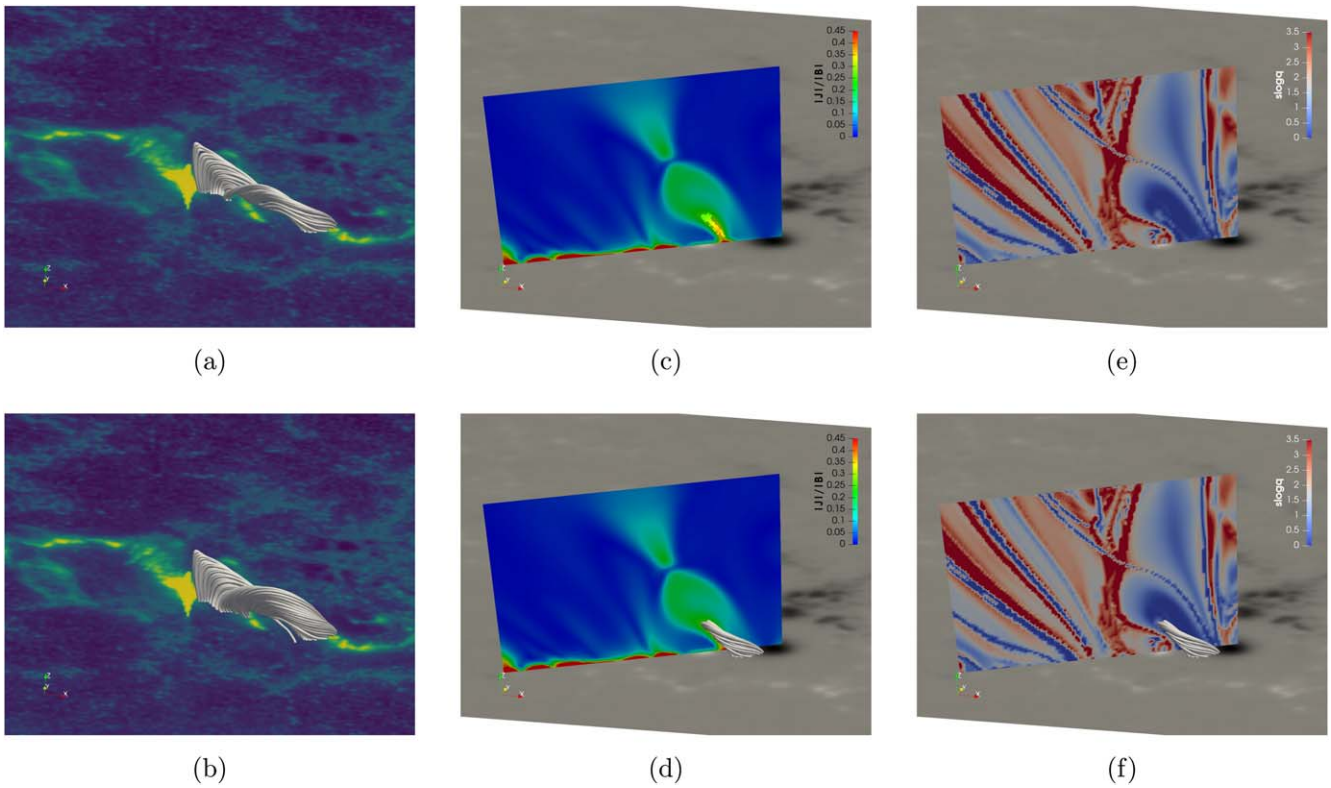

Figure 7. Enlarged and side views of the identified MFR in Figure 6(b) for the criteria of (a) $|T_w| > 1$ and (b) $|T_w| > 0.8$, and similarly for Figure 6(c), (c) the distribution of $|\boldsymbol{J}|/|\boldsymbol{B}|$ as indicated by the colorbar on a vertical slice across the identified MFR for $|T_w| > 1$ with the MFR field line intersection points colored by the corresponding values according to the colorbar, (d) same as (c) but overplotted with the MFR field lines, and (e)–(f) the distributions of the squashing degree Q on the same slices of (c) and (d).

The NLFFF extrapolation result by Zhao et al. (2016) demonstrated the existence of a strongly twisted MFR, which used magnetograms at different times from ours as the input and an alternative method to process the boundary conditions. Kilpua et al. (2021) used a data-driven magnetofrictional method that was driven by several days of time-varying magnetograms, and thus the underlying model and approach are different from ours. To obtain the MFR topology, they also needed to adjust the free parameters related to the injection of twist at the bottom boundary. On the other hand, it has been found that there is no twisted MFR but two J-shaped sheared arcades and overlying arcades based on the line-of-sight photospheric magnetogram before the flare using the flux rope insertion method, which is consistent with our result (Liu et al. 2018; Shen et al. 2022). So it is generally understood that different studies can yield different results owing to the different numerical methods and boundary conditions employed. One unique aspect in our study is that we intend to compare with an additional analysis of the interplanetary counterparts of the CME-MFRs based on in situ measurements, which provides support for the physical interpretations we present and the reliability of our results.

4. Estimation of Magnetic Properties of MFRs

After the identification of MFRs on the Sun for the two events, we look further into the magnetic properties of MFRs at different stages or locations and try to find a potential correlation among them. For example, the total magnetic flux (generally considered conserved) is one of the most important quantitative properties of MFRs that can be measured or derived to make a connection between the CME-MFR and the corresponding ICME/MC (Qiu et al. 2007; Hu et al. 2014).

Specifically, for the identified preexisting MFR in event 1, we give below a quantitative description of the magnetic properties. The axial magnetic flux enclosed by the preexisting MFR's footpoints is calculated for further analysis. The regions of the footpoints are obtained by extracting the intersection points between the field lines from the MFR and a slice parallel to the bottom boundary (photosphere). We choose a slice at a height of 1″, where two well-separated groups of footpoints are obtained. In general, more grid points are included under a smaller $|T_w|$ threshold value for the MFR criterion, i.e., more points with $|T_w|$ exceeding such a value. Here we denote the region dominated by the positive magnetic field in the MFR footpoints as "FP_+" and the region taken up mainly by the negative magnetic field in the MFR footpoints as "FP_-". The total axial (or toroidal) magnetic flux for both regions is calculated based on $\Phi_z = \iint B_z dS$, where B_z is the vertical magnetic field component. After the two well-separated groups of footpoints are obtained, the integration is estimated by summing the magnetic flux from all grid points (pixels) within the identified footpoint regions on the slice.

Table 3 shows the result of flux calculations of the identified MFR. The differences in Φ_z between FP_+ and FP_- are within one order of magnitude for different T_w criteria, though they get smaller for a higher $|T_w|$ threshold. Given that the largest Φ_z in terms of magnitude is still significantly smaller than the reconnection flux measured from the flare ribbons after the eruption, especially for the typical criterion $|T_w| > 1.0$, we believe that the MFR found from the extrapolation is likely a seed MFR before the eruption. It should be noted that the

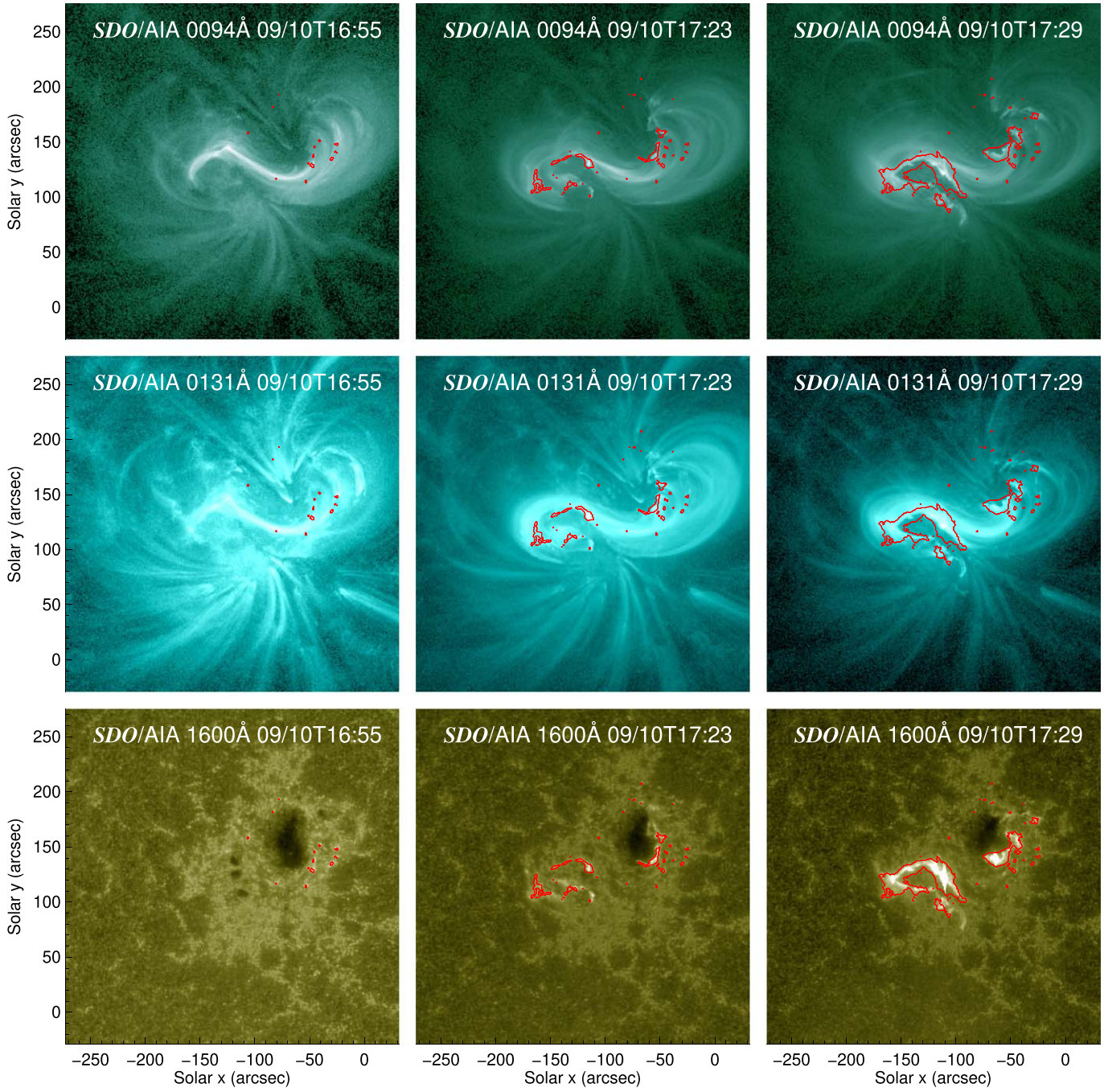

Figure 8. Observations from SDO/AIA in 94 Å, 131 Å, and 1600 Å (from top to bottom row) wavelength channels of AR 12158 for event 2. The format is the same as that of Figure 4.

difference in fluxes for the positive and negative footpoint regions' results exists because the field lines originating from the footpoints in one region that we identify mainly based on the $|T_w|$ threshold condition do not all end in the other polarity region. In this case, the flux is larger in the negative footpoint region than in the positive region since one group of footpoints (FP_-) is located closer to one main negative polarity of the magnetogram than the other group of footpoints (FP_+) is to any main positive polarity. And FP_- takes up a rather smaller area compared to FP_+, but the latter has a much lower average magnetic field $\langle B_z \rangle$, current density $\langle J_z \rangle$, and total current I_z.

A summary of the quantitative results for the MFRs in the two events is given in Table 4. The corresponding in situ modeling results for the two events are provided by Hu et al. (2021a) by applying two MC reconstruction methods. One of the modeling methods is the Grad–Shafranov reconstruction technique yielding a 2D configuration of the MFR (Hu & Sonnerup 2002; Hu 2017). The other method is the optimization approach based on a more general linear force-free formulation to obtain a more complex quasi-3D structure (Hu et al. 2021a, 2021b). For event 1, the twist of the MFR identified in the source region is relatively consistent with the in situ modeling results of the MFR structure, considering the uncertainty of the total twist numbers. The axial magnetic flux calculated from the in situ modeling results is significantly larger than the seed MFR identified in the source region before

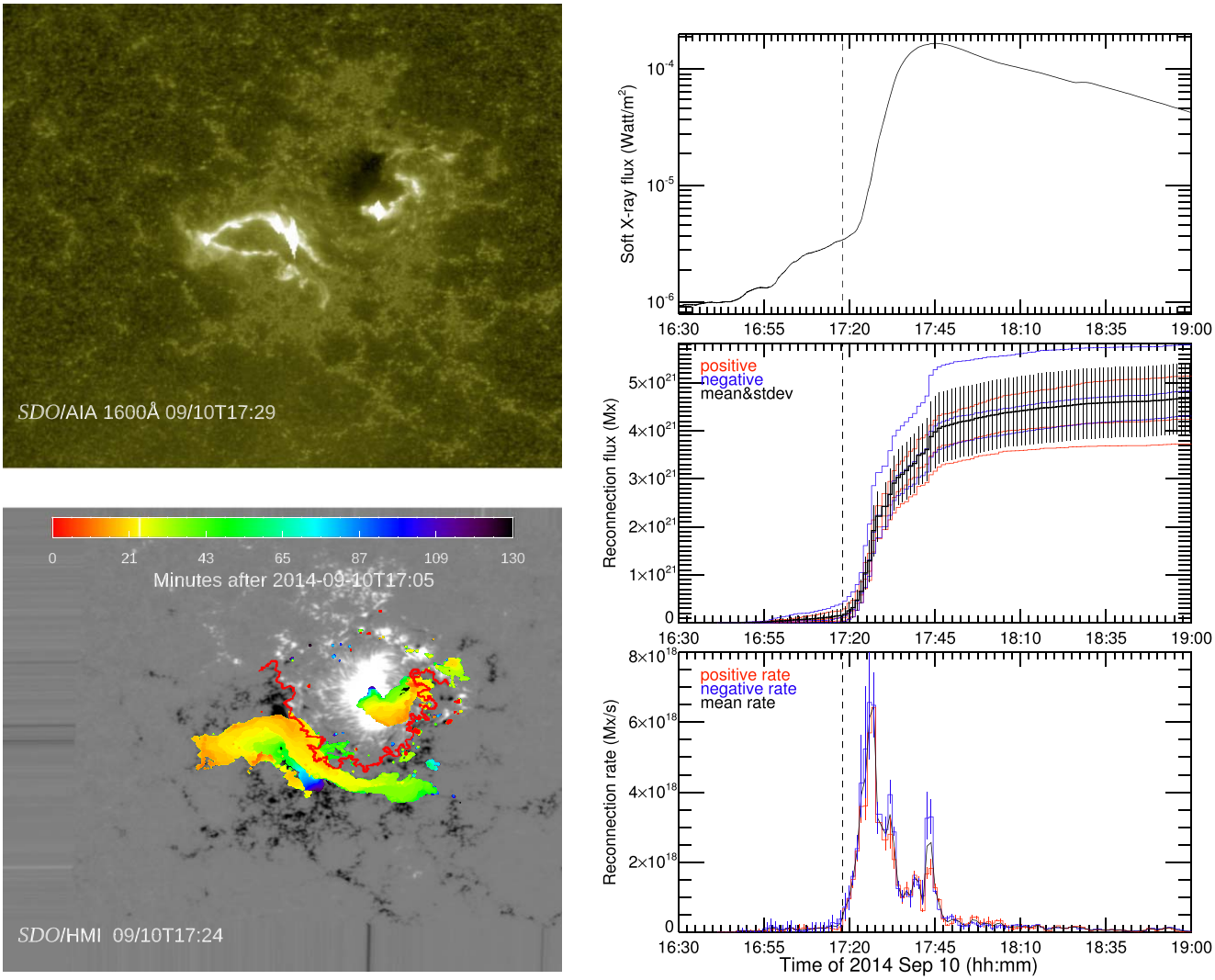

Figure 9. The observations of flare ribbons and measurements of the reconnection flux for event 2. The format is the same as that of Figure 5.

the eruption, while the reconnection flux measured from the source region after the eruption is generally larger than the axial flux from the in situ modeling results. The poloidal magnetic flux, obtained from the in situ modeling results, appears to agree better with the reconnection flux, subject to the uncertainty in the axial length. Specifically if one assumes a typical axial length $\in$ [1, 2] au (see Hu et al. 2015) for an MC flux rope, this amounts to a total poloidal flux in the range 9.2–18 $\times$ 10^{20} Mx for event 1, based on the 2D MC modeling result.

For event 2, the axial (toroidal) flux content from the in situ 3D model agrees with the reconnection flux within their respective uncertainty ranges. Other parameters in the source region are not available (marked by "...") since we do not find a preexisting MFR structure before the eruption. The 2D MC model also fails to yield an acceptable solution. The twist of the MFR from the in situ modeling is generally larger than the twist we find in the groups of field lines in Figure 10 (the maximum $|T_w| \sim 0.97$). A CME-MFR containing a significant amount of flux is likely formed during eruption through a dynamic evolution process in the solar atmosphere. Recently this was demonstrated by unique observational analysis and data-inspired numerical simulation (Xing et al. 2020; Jiang et al. 2021a) for the "increase-to-decrease" behavior in the toroidal flux of a CME-MFR. However the applicability of such analysis to our events is beyond the scope of the current study. To study such a process usually requires discerning multiple flux systems with complex and constantly evolving topologies. And it remains a challenge to separate the toroidal and poloidal flux contents from the reconnection flux, although the pioneering approach developed by Qiu (2009) for detailed analysis of the reconnection sequence can help in future studies.

5. Conclusions

In this paper, we identify MFR structures in solar source regions and establish the connection between MFRs on the Sun and their in situ counterparts quantitatively for two selected events. One event began on 2013 April 11 (event 1, AR 11719) and the other on 2014 September 10 (event 2, AR 12158). Each event exhibits a sequence of flare, CME, and the corresponding ICME observed by multiple spaceborne instruments. We perform coronal magnetic field extrapolations for each AR by the CESE-MHD-NLFFF method, which utilizes preprocessed photospheric magnetograms, and the results are also examined through a set of convergence metrics. Remote-sensing observations from SDO are

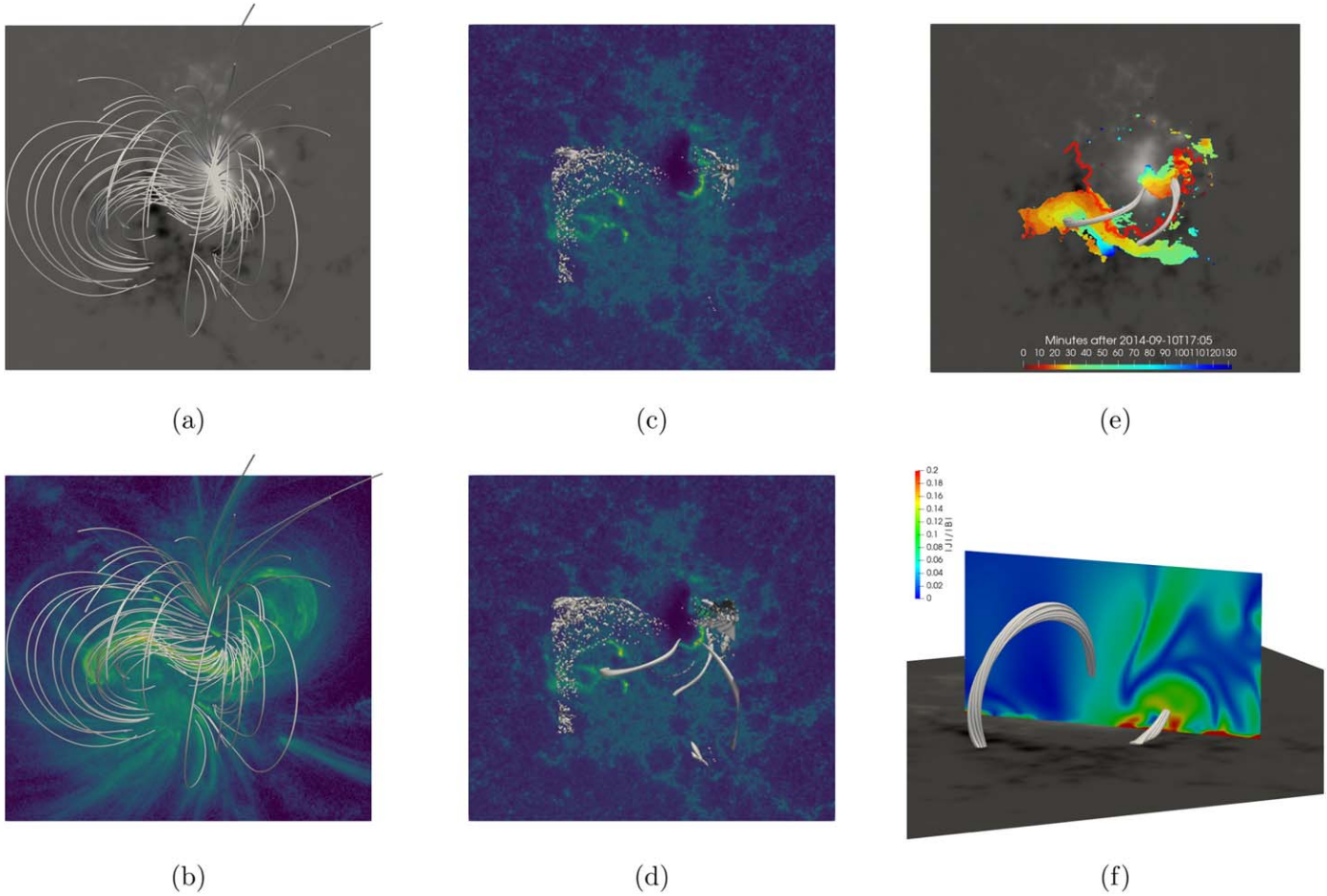

Figure 10. Magnetic field topology analysis for event 2: (a)–(b) selected field lines superimposed on the B_z map and an AIA 131 Å image at 17:00 UT, respectively; the isosurfaces of (c) $T_w = -1$ and (d) $T_w = -0.8$ over the background of the AIA 1600 Å observation at 17:23 UT; (e) selected field line bundles based on the threshold condition $|T_w| > 0.8$ with a composite background of the B_z map and color-coded flare ribbons (the same as the bottom left panel in Figure 9); and (f) the distribution of $|\boldsymbol{J}|/|\boldsymbol{B}|$ on a vertical slice intersecting the two field line bundles in (e).

analyzed to find evidence of MFRs and trace the evolution of the associated flares. Specifically we measure the amount of magnetic reconnection flux by analyzing the temporal and spatial evolution of flare ribbons. We combine the extrapolation results with observations to identify MFRs on the Sun before the eruption and estimate their magnetic properties. The main results of our study are summarized as follows.

1. Observational evidence of MFR footpoints and associated magnetic reconnection flux during the flare eruption is inferred from multiwavelength observations. From the comparison among EUV observations, there are signs of MFRs for the two events. Based on the flare ribbon measurements, the total magnetic reconnection flux reaches $17 \pm 2.8 \times 10^{20}$ Mx for event 1, and $47 \pm 7.5 \times 10^{20}$ Mx for event 2, which correspond to the amount of available flux to be injected into the final CME-MFRs.
2. From the combination of extrapolation and observation results, a coherent MFR structure before the flare eruption is identified for event 1. However, there is no preexisting MFR found for event 2, based on the same set of MFR criteria, including the requirement for the field line twist number to be $|T_w| > 1.0$ and for both regions of the MFR field line footpoints to be close to the main flare ribbons. For event 1, a coherent preeruption MFR is determined, which carries a maximum $T_w = -1.5$, and its two ends are located near the opposite ends of the respective flare ribbons across the PIL.
3. The magnetic properties of MFRs on the Sun are summarized and compared with the corresponding in situ modeling results from Hu et al. (2021a) in Table 4. For event 1, the axial magnetic flux from the in situ modeling results is in the order of 10^{20}–10^{21} Mx, while the total magnetic reconnection flux after the eruption from the source region is in the order of $\sim 10^{21}$ Mx. Both are significantly larger than the flux in the identified preexisting MFR's footpoint areas, which is in the order of 10^{19}–10^{20} Mx.
4. For event 2, there is no preexisting MFR identified. The amount of magnetic reconnection flux, $47 \pm 7.5 \times 10^{20}$ Mx, agrees with the corresponding ICME MFR toroidal flux, $\sim$16–81 $\times$ 10^{20} Mx, within the limits of the uncertainty ranges.

These results for the two events indicate the dynamic and complex nature of an MFR's formation during its evolution process while some properties (like magnetic flux and twist) are useful for making connections between the formation of MFRs on the Sun and their in situ characteristics in a quantitative manner. Based on these quantitative results, we conclude that the magnetic reconnection process, manifested during solar

Table 3
Magnetic Properties of the Footpoint Regions Associated with an MFR in AR 11719 for Event 1 with Different Criteria at $z = 1.''0$

		Φ_z (10^{20} Mx)	# of Grids	$\langle B_z\rangle$ (G)	$\langle J_z\rangle$ (10^{-3} A m^{-2})	I_z (10^{10} A)
			$\lvert T_w\rvert > 0.8$			
FP_+	(+)	0.510	165	58.2	−0.79	−6.9
	(−)	0				
FP_-	(+)	0	64	−394	5.8	20
	(−)	−1.34				
			$\lvert T_w\rvert > 0.9$			
FP_+	(+)	0.385	114	63.6	−0.60	−3.6
	(−)	0				
FP_-	(+)	0	48	−367	5.8	15
	(−)	−0.934				
			$\lvert T_w\rvert > 1.0$			
FP_+	(+)	0.283	68	78.5	−0.19	−0.68
	(−)	0				
FP_-	(+)	0	35	−343	5.8	11
	(−)	−0.638				

Notes. The Φ_z column shows the sum of normal magnetic flux over all associated grids for each group of identified footpoints; the fourth column shows the number of grids on the chosen slice containing the identified footpoints; $\langle B_z\rangle$ denotes the average vertical magnetic field for each group of footpoints; $\langle J_z\rangle$ denotes the average current density in the z direction for each group of footpoints, $J_z = \frac{(\nabla\times \boldsymbol{B})_z}{\mu_0}$; and $I_z = \Sigma\ (J_z dS)$ denotes the total current in the z direction for each group. (+): positive flux; (−): negative flux.

Table 4
Summary of Magnetic Properties for MFRs in Two Events

Parameter (all fluxes in 10^{20} Mx)	Source Region Results	In Situ Modeling Results[a]	
		2D	3D
	Event 1: 2013-04-11		
Axial flux Φ_z	0.3–1.3[b]	5.7	8.9–14
Twist τ	∼1.5[b] (axis)	1.6/au	0.84–1.1/au
Reconnection flux[c]	17 ± 2.8	...	...
Poloidal flux	...	9.2/au	10–12/au
	Event 2: 2014-09-10		
Axial flux Φ_z	...	...	16–81
Twist τ	...	...	1.0–2.4/au
Reconnection flux[c]	47 ± 7.5	...	...
Poloidal flux	...	...	38–81/au

Notes.
[a] In situ modeling results of MCs cited from Hu et al. (2021a). For the 3D model, the poloidal flux is approximated by $\tau\Phi_z$.
[b] Parameters for identified "preexisting" MFR only.
[c] The reconnection flux is estimated based on Figures 5 and 9.

flares, injects a significant amount of magnetic flux into the ensuing CME-MFR. For event 1, the identified preexisting (or preeruption) MFR from the NLFFF extrapolation is likely a seed MFR before the eruption and additional flux is injected through the magnetic reconnection process associated with the flare. Furthermore, based on the comparison among various interrelated magnetic flux contents and the corresponding flare ribbon morphology for each event, we conclude that for event 1, a quasi-2D configuration of the MFR is largely valid, for which the poloidal flux is more meaningfully defined and compared more favorably with the corresponding reconnection flux than the axial flux. For event 2, however, we believe that the MFR topology deviates more from a 2D configuration and is better described by a quasi-3D model for which the axial flux agrees with the reconnection flux. In this case, the poloidal flux is not readily defined geometrically because there does not exist a straight field line representing the central axis of a flux rope (see Hu et al. 2021a). Therefore, for the 3D model, we choose to approximate the poloidal flux by the product of the average field line twist and the axial flux (see, e.g., Hu et al. 2014).

This study represents an effort to make a physical connection between a solar MFR (including the MFR before and after the eruption) and the corresponding ICME/MC by quantitative comparison of the magnetic properties under different scenarios through extrapolations and observations. It is usually not easy to envisage the existence of a coherent preexisting MFR, reconstruct it before the eruption in the solar source region for a CME event, and make a one-to-one connection with its interplanetary counterpart. Efforts have been made continuously on the quantitative description of the MFR configuration with more advanced observations and improved numerical simulation techniques, which is helpful for further understanding the formation and evolution processes of CME-MFRs. Future studies including more events will be carried out for a deeper understanding of CME-MFRs, where improvements to the extrapolation method and use of high-resolution ground-based data can be implemented.

W.H. and Q.H. acknowledge support from National Science Foundation grants AGS-1954503 and AGS-1650854 and the NSO/DKIST Ambassador Program. Q.H. also acknowledges partial support from AGS-2020703. C.J. acknowledges support from the National Natural Science Foundation of China (NSFC 42174200 and 41822404), Fundamental Research Funds for the Central Universities (grant No. HIT.OCEF.2021033), and the Shenzhen Technology Project JCYJ20190806142609035. A.P. would like to acknowledge support from the Research Council of Norway through its 458 Centres of Excellence scheme, project No. 262622, and from Synergy grant No. 810218 459 (ERC-2018-SyG) of the European Research Council. The data for solar observations were provided by GOES, and the HMI and AIA instruments on board SDO (http://jsoc.stanford.edu/). The Wind spacecraft measurements can be accessed via NASA CDAWeb: https://cdaweb.gsfc.nasa.gov/index.html/.

Appendix
Convergence Metrics

The metrics for the convergence study of the computation during the iteration process are defined below. These include the residual of the field between two successive iteration steps n and $n-1$ ($n > 1$),

$$res^n(\boldsymbol{B}) = \sqrt{\frac{1}{3}\sum_{\delta=x,y,z}\frac{\sum_i (B^n_{i\delta} - B^{n-1}_{i\delta})^2}{\sum_i (B^n_{i\delta})^2}}, \tag{A1}$$

where the subscript i refers to the linear indices of grid points and runs over all grid points in the computational volume. We also estimate the force-freeness of the numerical result by a current-weighted metric, *CWsin*, which is defined by (equivalent to the

weighted sine of the angle between $\boldsymbol{J}$ and $\boldsymbol{B}$)

$$CWsin = \frac{\sum_i |\boldsymbol{J}_i|\sigma_i}{\sum_i |\boldsymbol{J}_i|};\ \sigma_i = \frac{|\boldsymbol{J} \times \boldsymbol{B}|_i}{|\boldsymbol{J}_i||\boldsymbol{B}_i|}. \tag{A2}$$

The other important parameters—the total magnetic energy $E_{\rm tot}$ and the divergence-free condition $\langle |f_i| \rangle$ (Wheatland et al. 2000; Metcalf et al. 2008)—are defined by

$$E_{\rm tot} = \sum_i \boldsymbol{B}_i^2 \Delta V_i,$$
$$\langle |f_i| \rangle = \frac{1}{M} \sum_i \frac{(\nabla \cdot \boldsymbol{B})_i}{6\,|\,\boldsymbol{B}_i\,|\,/(\Delta x)_i}, \tag{A3}$$

where Δx is the grid spacing, M refers to the total number of grid points contained, and $\Delta V_i = (\Delta x)_i \times (\Delta y)_i \times (\Delta z)_i$ represents a volume element.

Since the metric *CWsin* is not always reliable for evaluating force-freeness, two additional metrics are proposed (see Jiang et al. 2012; Duan et al. 2017) by analyzing the residual force in the extrapolation result. The residual force for the numerical "force-free" field consists of two parts, the Lorentz force and a force induced by a nonzero $\nabla \cdot \boldsymbol{B}$. The nonzero divergence of the field introduces a force $\boldsymbol{F} = \boldsymbol{B}\nabla \cdot \boldsymbol{B}$ parallel to the field line, which is unphysical and only results from numerical errors. To find a reference value for these two forces, the decomposition of the Lorentz force can be used:

$$(\nabla \times \boldsymbol{B}) \times \boldsymbol{B} = (\boldsymbol{B} \cdot \nabla)\boldsymbol{B} - \nabla(B^2/2). \tag{A4}$$

Here the first component is the magnetic tension force and the second component is the magnetic pressure gradient force. These two terms should be balanced for a force-free field. So another metric for force-freeness can be defined, for a chosen volume V, as

$$E_{\nabla \times \boldsymbol{B}} = \frac{1}{V} \int_V \frac{|\boldsymbol{B} \times (\nabla \times \boldsymbol{B})|}{|(\boldsymbol{B} \cdot \nabla)\boldsymbol{B}| + |\nabla(B^2/2|} \, dV. \tag{A5}$$

This equation is the same as Equation (10) proposed by Malanushenko et al. (2014). Similarly, one can define an additional metric for divergence-freeness by measuring the force induced by the nonzero $\nabla \cdot \mathbf{B}$ by

$$E_{\nabla \cdot \boldsymbol{B}} = \frac{1}{V} \int_V \frac{|\boldsymbol{B}(\nabla \cdot \boldsymbol{B})|}{|(\boldsymbol{B} \cdot \nabla)\boldsymbol{B}| + |\nabla(B^2/2|} \, dV. \tag{A6}$$

ORCID iDs

Wen He https://orcid.org/0000-0001-8749-1022
Qiang Hu https://orcid.org/0000-0002-7570-2301
Chaowei Jiang https://orcid.org/0000-0002-7018-6862
Avijeet Prasad https://orcid.org/0000-0003-0819-464X

References

Amari, T., Luciani, J. F., Aly, J. J., Mikic, Z., & Linker, J. 2003, ApJ, 585, 1073
Antiochos, S. K., DeVore, C. R., & Klimchuk, J. A. 1999, ApJ, 510, 485
Aulanier, G., & Dudík, J. 2019, A&A, 621, A72
Aulanier, G., Janvier, M., & Schmieder, B. 2012, A&A, 543, A110
Berger, M. A., & Prior, C. 2006, JPhA, 39, 8321
Bobra, M. G., Sun, X., Hoeksema, J. T., et al. 2014, SoPh, 289, 3549
Burlaga, L. F. 1992, JGR, 97, 4283
Carmichael, H. 1964, NASSP, 50, 451
Chen, P. F. 2011, LRSP, 8, 1
Cheng, X., & Ding, M. D. 2016, ApJS, 225, 16
Cheng, X., Ding, M. D., & Fang, C. 2015, ApJ, 804, 82
Cheng, X., Guo, Y., & Ding, M. 2017, ScChD, 60, 1383
Chiu, Y. T., & Hilton, H. H. 1977, ApJ, 212, 873
De Rosa, M. L., Schrijver, C. J., Barnes, G., et al. 2009, ApJ, 696, 1780
Demoulin, P., Henoux, J. C., Priest, E. R., & Mandrini, C. H. 1996, A&A, 308, 643
Duan, A., Jiang, C., He, W., et al. 2019, ApJ, 884, 73
Duan, A., Jiang, C., Hu, Q., et al. 2017, ApJ, 842, 119
Fan, Y. 2001, ApJL, 554, L111
Forbes, T. G., & Priest, E. R. 1984, SoPh, 94, 315
Gary, G. A. 1989, ApJS, 69, 323
Gary, G. A. 2001, SoPh, 203, 71
Gibson, S. E., Fan, Y., Török, T., & Kliem, B. 2006, SSRv, 124, 131
Gopalswamy, N., Akiyama, S., Yashiro, S., & Xie, H. 2018, JASTP, 180, 35
Gopalswamy, N., Yashiro, S., Akiyama, S., & Xie, H. 2017, SoPh, 292, 65
Guo, Y., Xia, C., & Keppens, R. 2016, ApJ, 828, 83
Hirayama, T. 1974, SoPh, 34, 323
Hu, Q. 2017, ScChD, 60, 1466
Hu, Q., He, W., Qiu, J., Vourlidas, A., & Zhu, C. 2021a, GeoRL, 48, e90630
Hu, Q., He, W., Zhao, L., & Lu, E. 2021b, FrP, 9, 407
Hu, Q., Qiu, J., Dasgupta, B., Khare, A., & Webb, G. M. 2014, ApJ, 793, 53
Hu, Q., Qiu, J., & Krucker, S. 2015, JGRA, 120, 5266
Hu, Q., & Sonnerup, B. U. Ö. 2002, JGRA, 107, 1142
Inoue, S., Kusano, K., Büchner, J., & Skála, J. 2018, NatCo, 9, 174
Jiang, C., Chen, J., Duan, A., et al. 2021a, FrP, 9, 575
Jiang, C., Feng, X., Liu, R., et al. 2021b, NatAs, 5, 1126
Jiang, C., Cui, S., & Feng, X. 2012, Comput. Fluids, 54, 105
Jiang, C., & Feng, X. 2012, ApJ, 749, 135
Jiang, C., & Feng, X. 2013, ApJ, 769, 144
Jiang, C., & Feng, X. 2014, SoPh, 289, 63
Jiang, C., Feng, X., Fan, Y., & Xiang, C. 2011, ApJ, 727, 101
Jiang, C., Feng, X., Wu, S. T., & Hu, Q. 2012, ApJ, 759, 85
Jiang, C., Wu, S. T., Feng, X., & Hu, Q. 2014, ApJL, 786, L16
Jing, J., Liu, C., Lee, J., et al. 2018, ApJ, 864, 138
Joshi, B., Kushwaha, U., Veronig, A. M., et al. 2017, ApJ, 834, 42
Kaiser, M. L., Kucera, T. A., Davila, J. M., et al. 2008, SSRv, 136, 5
Kazachenko, M. D., Lynch, B. J., Welsch, B. T., & Sun, X. 2017, ApJ, 845, 49
Kilpua, E. K. J., Pomoell, J., Price, D., Sarkar, R., & Asvestari, E. 2021, FrASS, 8, 35
Kopp, R. A., & Pneuman, G. W. 1976, SoPh, 50, 85
Lemen, J. R., Title, A. M., Akin, D. J., et al. 2012, SoPh, 275, 17
Liu, R. 2020, RAA, 20, 165
Liu, R., Kliem, B., Titov, V. S., et al. 2016, ApJ, 818, 148
Liu, T., Su, Y., Cheng, X., van Ballegooijen, A., & Ji, H. 2018, ApJ, 868, 59
Longcope, D., Beveridge, C., Qiu, J., et al. 2007, SoPh, 244, 45
Low, B. C., & Lou, Y. Q. 1990, ApJ, 352, 343
MacNeice, P., Olson, K. M., Mobarry, C., de Fainchtein, R., & Packer, C. 2000, CoPhC, 126, 330
Magara, T. 2004, ApJ, 605, 480
Malanushenko, A., Schrijver, C. J., DeRosa, M. L., & Wheatland, M. S. 2014, ApJ, 783, 102
Metcalf, T. R., Jiao, L., McClymont, A. N., Canfield, R. C., & Uitenbroek, H. 1995, ApJ, 439, 474
Metcalf, T. R., De Rosa, M. L., Schrijver, C. J., et al. 2008, SoPh, 247, 269
Moore, R. L., Sterling, A. C., Hudson, H. S., & Lemen, J. R. 2001, ApJ, 552, 833
Pesnell, W. D., Thompson, B. J., & Chamberlin, P. C. 2012, SoPh, 275, 3
Priest, E. R., & Longcope, D. W. 2017, SoPh, 292, 25
Qiu, J. 2009, ApJ, 692, 1110
Qiu, J., Hu, Q., Howard, T. A., & Yurchyshyn, V. B. 2007, ApJ, 659, 758
Qiu, J., Lee, J., Gary, D. E., & Wang, H. 2002, ApJ, 565, 1335
Qiu, J., Liu, W., Hill, N., & Kazachenko, M. 2010, ApJ, 725, 319
Qiu, J., Wang, H., Cheng, C. Z., & Gary, D. E. 2004, ApJ, 604, 900
Schmieder, B., Aulanier, G., & Vršnak, B. 2015, SoPh, 290, 3457
Schou, J., Scherrer, P. H., Bush, R. I., et al. 2012, SoPh, 275, 229
Schrijver, C. J., DeRosa, M. L., Metcalf, T., et al. 2008, ApJ, 675, 1637
Shen, J., Ji, H., & Su, Y. 2022, RAA, 22, 015019
Sturrock, P. A. 1966, Natur, 211, 695
Sun, X., Hoeksema, J. T., Liu, Y., et al. 2012, ApJ, 748, 77
Thalmann, J. K., Wiegelmann, T., & Raouafi, N. E. 2008, A&A, 488, L71
Titov, V. S., & Démoulin, P. 1999, A&A, 351, 707
Titov, V. S., Hornig, G., & Démoulin, P. 2002, JGRA, 107, 1164
van Ballegooijen, A. A., & Mackay, D. H. 2007, ApJ, 659, 1713
van Ballegooijen, A. A., & Martens, P. C. H. 1989, ApJ, 343, 971

Vemareddy, P. 2021, FrP, 9, 605
Vemareddy, P., & Zhang, J. 2014, ApJ, 797, 80
Wang, H., Cao, W., Liu, C., et al. 2015, NatCo, 6, 7008
Wheatland, M. S., & Régnier, S. 2009, ApJL, 700, L88
Wheatland, M. S., Sturrock, P. A., & Roumeliotis, G. 2000, ApJ, 540, 1150
Wiegelmann, T., Inhester, B., & Sakurai, T. 2006, SoPh, 233, 215
Wiegelmann, T., & Sakurai, T. 2021, LRSP, 18, 1
Wiegelmann, T., Thalmann, J. K., Inhester, B., et al. 2012, SoPh, 281, 37
Xing, C., Cheng, X., & Ding, M. D. 2020, Innov, 1, 100059
Zhao, J., Gilchrist, S. A., Aulanier, G., et al. 2016, ApJ, 823, 62
Zhu, C., Qiu, J., Liewer, P., et al. 2020, ApJ, 893, 141